AIAA JOURNAL
Vol. 48, No. 11, November 2010

Microramp Flow Control of Normal Shock/Boundary-Layer Interactions

Thomas Herges,* Erik Kroeker,* Greg Elliott,† and Craig Dutton‡
University of Illinois at Urbana-Champaign, Urbana, Illinois 61801

DOI: 10.2514/1.J050313

Boundary-layer bleed has conventionally been used to control separation due to shock wave/boundary-layer interactions within supersonic engine inlets. However, bleed systems result in a loss of captured mass flow, incurring higher drag and, ultimately, lower propulsion system efficiency. Microramp sub-boundary-layer vortex generators arranged in a spanwise array have been proposed in the past as a form of flow-control methodology for shock wave/boundary-layer interactions. Experiments have been conducted herein at Mach 1.4 to characterize flow details of such devices and obtain quantitative measurements of their ability to control the interaction of a normal shock with a turbulent boundary layer. The flowfield was analyzed using schlieren photography, surface oil flow visualization, pressure-sensitive paint, and particle image velocimetry. An array of three microramps, for which the height was scaled to 36% of the incoming boundary-layer thickness, was placed ahead of the normal shock interaction. It was demonstrated that the microramps did entrain higher-momentum fluid into the boundary layer, which improved boundary-layer health. Specifically, the incompressible displacement thickness, momentum thickness, and shape factor were decreased, and the skin friction coefficient was increased, for the shock wave/boundary-layer interaction with the microramp array relative to the no-array case.

Nomenclature

A_p	=	microramp angle of incidence
C_f	=	skin friction coefficient, $\tau_w/[(1/2)\rho_e u_e^2]$
c	=	microramp chord length, mm
d	=	distance from camera lens to calibration scale, mm
H	=	incompressible boundary-layer shape factor, δ^*/θ
H_{tr}	=	transformed form factor
h	=	microramp height, mm
L	=	length of scale used for calibration, pixels
l	=	length of scale used for calibration, mm
M	=	Mach number
N	=	number of samples
p	=	static pressure, kPa
s	=	spanwise microramp spacing, mm
t	=	time, s
U	=	mean freestream velocity in streamwise direction, m/s
u	=	mean velocity in streamwise direction, m/s
u_τ	=	wall-friction velocity, $(\tau_w/\rho_w)^{1/2}$, m/s
u^+	=	mean velocity in streamwise direction in wall coordinates, u/u_τ
u'	=	standard deviation of velocity in streamwise direction, m/s
$u'v'$	=	Reynolds shear stress, m^2/s^2
v'	=	standard deviation of velocity in transverse direction, m/s
w	=	uncertainty value
Xp	=	distance between normal shock and microramp array, mm
x	=	streamwise coordinate, mm
y	=	transverse coordinate, mm
y^+	=	transverse wall coordinate, yu_τ/ν_w
z	=	spanwise coordinate, mm
z_c	=	confidence coefficient
δ	=	boundary-layer thickness, mm
δ^*	=	boundary-layer incompressible displacement thickness, mm
θ	=	boundary-layer incompressible momentum thickness, mm
ν	=	kinematic viscosity, m^2/s
Π	=	coefficient of wake function
ρ	=	density, kg/m^3
σ	=	standard deviation
τ	=	shear stress, kPa

Subscripts

e	=	conditions at the edge of the boundary layer
w	=	conditions at the wall

Presented as Paper 2009-0920 at the 47th AIAA Aerospace Sciences Meeting, Orlando, FL, 5–8 January 2009; received 25 October 2009; revision received 9 July 2010; accepted for publication 11 July 2010.

*Graduate Research Assistant, Aerospace Engineering, 104 South Wright Street. Student Member AIAA.

†Professor and Associate Head, Aerospace Engineering, 104 South Wright Street. Associate Fellow AIAA.

‡Bliss Professor and Head, Aerospace Engineering, 104 South Wright Street. Associate Fellow AIAA.

I. Introduction

A CRITICAL issue with the design of any supersonic inlet is the shock wave/boundary-layer interactions (SBLIs) that occur. In a supersonic inlet, air is decelerated by a series of shock structures, usually terminating in a normal shock. As a result, the growing boundary layer along the wall of the inlet will experience adverse pressure gradients, possibly resulting in boundary-layer separation and even engine unstart. Bleed systems, which extract low-momentum fluid from the boundary layer, have been demonstrated to reduce both boundary-layer thickness and the severity of separation [1]. However, bleed systems result in a loss of captured mass flow [2]. The reduction in captured mass flow results in the necessity for larger inlets, incurring higher drag and, ultimately, lower propulsion system efficiency.

To control SBLIs, several flow-control methods have been proposed in addition to boundary-layer bleed systems. Early investigation into SBLI control focused on two-dimensional surface features that aimed to spread out the bifurcated lambda foot of the normal shock. A lambda shock decelerates the flow through a pair of oblique shocks, thus having a smaller total pressure loss than a single normal shock with the same static pressure rise. This approach to

SBLI control was investigated using a variety of methodologies including porous surfaces [3] and two-dimensional bumps [4]. While two-dimensional surface features like bumps proved effective at spreading the lambda foot of the normal shock, the large surface features increased drag.

Further investigation into SBLI control applied arrays of discrete three-dimensional surface features. Investigations of arrays of streamwise slots demonstrated that they were able to create the same bifurcated lambda structure as two-dimensional features when placed under an SBLI [5]. Of particular interest is that the lambda shock structure extended between the slots as well [6]. Thus, a series of three-dimensional surface features was demonstrated to be able to control the SBLI over a two-dimensional region [7]. With respect to the control effectiveness of two-dimensional features like bumps, this suggested that the flow control could be broken up into discrete arrays of three-dimensional features. Therefore, the flow-control benefit of a two-dimensional bump could be achieved with a smaller drag penalty [8].

Upon further investigation into the arrays of three-dimensional geometries for SBLI control, sub-boundary-layer vortex generators (SBVGs) demonstrated promise for reducing boundary-layer growth and eliminating or reducing separation when placed upstream of the SBLI [9,10]. By contrast to previously discussed control methods, SBVGs aim to control SBLIs by energizing the boundary layer and making it less susceptible to shock-induced separation. Like traditional vortex generators, SBVGs entrain higher-momentum fluid to energize the low-momentum fluid near the wall to improve boundary-layer health and suppress or delay separation. Because of their smaller size, SBVGs have been shown to have significantly reduced device drag compared with conventional vortex generators [11].

One SBVG geometry that has been of particular interest is the microramp. The microramp has demonstrated the capability to reduce separation region length and reduce boundary-layer thickness while being physically robust and easy to machine [12,13]. While microramps did not completely eliminate boundary-layer separation in the previous experiments, they could break up separation regions in the vicinity directly behind the microramp [13]. Therefore, like the three-dimensional bump, an array of microramps would be needed in order to control the SBLI for an entire supersonic inlet. The spacing of such an array has been previously proposed [10].

The microramp geometry has been optimized in earlier investigations to minimize the transformed form factor (H_{tr}) and, separately, to maximize the total pressure difference downstream of the SBLI [10]. It was found that, when the microramp geometry was optimized for one criterion, the other criterion suffered. Three optimized geometries scaled by microramp height were derived, one for each criterion separately and one for which each criterion was equally weighted [10]. These optimized geometries have been the focus of several recent investigations [1,12–14].

In the present study, the normal SBLI downstream from a microramp array geometry optimized for transformed form factor has been characterized. The array was investigated in a Mach 1.4 flow, for which the SBLI is incipiently separated, meaning that the flow is just on the edge of separation. The flowfield is analyzed using schlieren photography, surface flow visualization, pressure-sensitive paint (PSP), and particle image velocimetry (PIV).

II. Experimental Setup

A supersonic blowdown wind tunnel designed for Mach 1.4 was used to study the flow over and around a microramp array, as well as the array's effect on a normal shock/boundary-layer interaction. The cross-sectional area of the test section of the wind tunnel without the microramp array measures 63.5 mm in height and width. The test section has a length of 416 mm. The tunnel has windows in each side wall, providing optical access for schlieren photography and PIV, and a smaller window in the top wall for surface flow visualization and PSP viewing, as well as a small window in the bottom wall for PIV laser sheet access (see Fig. 1; bottom wall window not shown). The air supply for the wind tunnel is an Ingersoll–Rand compressor with a 34 $m^3/$ min. flow rate at 1 MPa pressure. The wind tunnel is capable of running longer than 20 min. The tunnel is controlled by both a pneumatic valve, with a Fisher TL 101 process controller, and a manual gate valve. The stagnation pressure and total temperature of the wind tunnel at the operating conditions of these experiments are 206.8 ± 0.7 kPa and 301 K, respectively. The incoming boundary layer is 4.77 mm thick, as determined by PIV, and the unit Reynolds number is 30.4×10^6 m^{-1}. There are three pressure transducers: one for the supply tank, one for the tunnel stagnation pressure, and one for the static pressure in the test section. The supply tank and tunnel stagnation pressure measurements are made with Ashcroft K1 transducers with 1% full-scale accuracy. The static pressure measurements in the test section are made with an Omega PX209-015A5V transducer with 1.5% full-scale accuracy. A thermocouple mounted in the contraction section of the tunnel measures the stagnation temperature. A schematic of the wind tunnel along with the position of the microramp array is shown in Fig. 1.

The dimensions used for the microramp array examined were based on the optimized geometries from [10] and are listed in Table 1, as well as shown in Fig. 1a. These dimensions were obtained by minimizing the transformed form factor (H_{tr}) as explained in [10], based on a design-of-experiments response surface methodology study of 27 unique computational fluid dynamics (CFD) cases varying the A_p, h, c, s, and Xp parameters of the microramp array. The CFD simulations used the Reynolds-averaged Navier–Stokes WIND code with a grid containing 263,552 mesh points [10].

The microramp array was machined into an insert that could be replaced with a blank for measurements of the normal shock/boundary-layer interaction without the microramp array.

The normal shock was held in place with a 5 deg expansion of the upper wind-tunnel wall that continued for 114.3 mm in the x direction before ending with a lip; this expansion is referred to as the shock holder. The shock holder location with respect to the wind tunnel is shown in Fig. 1b. The shock holder held the normal shock at an average Xp/δ value of 12.8 (dimensionally, 61.2 mm), from half the chord length of the microramp array to the normal shock position, with a standard deviation of 3.5 mm as compared with the target Xp/δ value of 12.65. This is a 1.2% difference in shock location from the designed value, but the effects of the microramp array are not strongly sensitive to shock location, and a complete sensitivity analysis on the effects of varying normal shock position is outside the scope of this investigation [15]. This is equivalent to the normal shock lying at a distance of 66.6 mm from the front edge of the microramp array. Without the microramp array, the normal shock was held with a standard deviation of 5.3 mm.

Instantaneous schlieren images and surface flow visualizations were obtained of the microramp flow, as well as PSP and PIV measurements.

The schlieren optical setup was in a standard Z arrangement. Instantaneous schlieren photography was conducted using a Newport Corporation flashlamp model LM-1 pulsed at 10 Hz for a duration of 20 ns, a Quantum Composers model 9514 pulse generator, and a Xenon Corporation Nanopulser model 437B. The pulsed light was reflected through the test section using collimating mirrors and then focused to a point. Both collimating mirrors had a focal length of 1.6 m. The image was cut horizontally from below with a knife edge before passing into the PCO.1600 charge-coupled device (CCD) camera manufactured by Cooke, Inc.

The surface oil used for the surface flow visualization is one part oleic acid, five parts titanium dioxide, and 10 parts silicone oil. Images of the microramp and surface oil flow were obtained through the window in the top of the wind tunnel, while the images of the shock/boundary-layer interaction region were acquired through the large side windows. The same PCO.1600 CCD camera used for schlieren photography was used to obtain the surface flow visualization images.

The PSP used was Uni-Fib, manufactured by Innovative Scientific Solutions, Inc. Images of the microramp array and PSP intensity signal were obtained in the same manner as the images for the surface flow visualizations. The same PCO.1600 CCD camera used for schlieren photography was used to obtain the PSP images. The illumination source is a blue light-emitting diode (LED) lamp with a

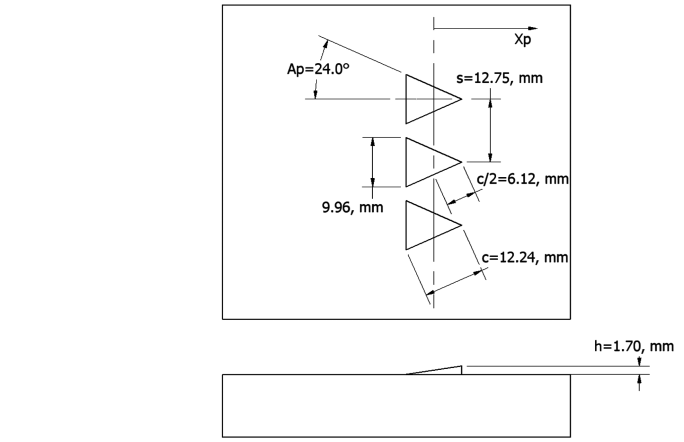

a)

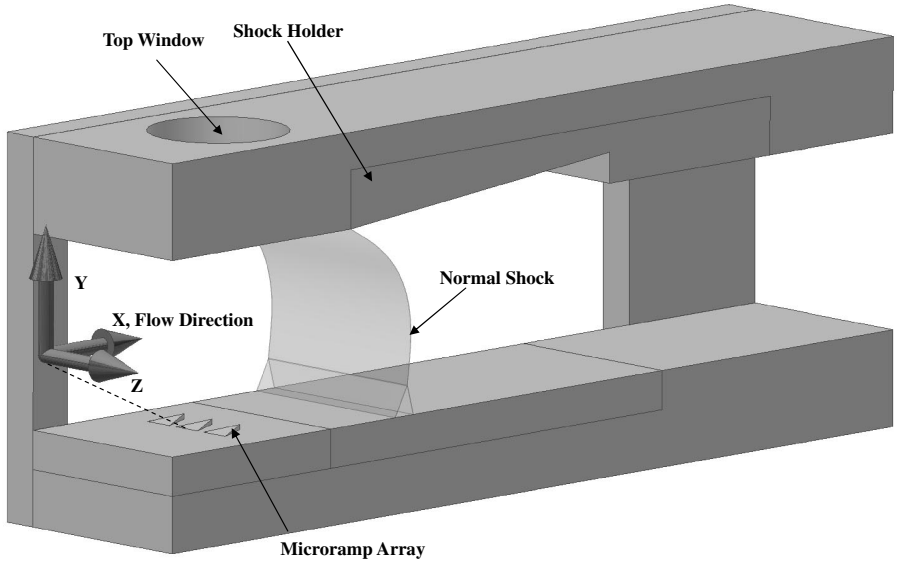

b)

Fig. 1 Experimental schematics: a) microramp array and b) wind tunnel.

low-pass filter placed on the lamp, so that the incident light in the range of the luminescent signal wavelength is mostly filtered. The PCO.1600 CCD camera was fitted with a 610 nm high-pass filter, so that the glare of the LED illumination source is reduced, and only the luminescent signal is collected. Five pressure-tap holes were drilled into and near the microramp array, as well as along the normal shock/boundary-layer interaction region. The locations of the pressure taps, both around the microramp array and normal shock position, were chosen to contain pressure values over a range of $0.4 p/p_{\text{inf}}$ in order to minimize the errors from the calibration curves. While the tunnel was running, the pressure-tap values were read by the Omega PX209-015A5V transducer and recorded for PSP image calibration in addition to obtaining images of the illuminated surface. The PSP images collected were the result of averaging long-exposure images. Both calibration curves used a second-order polynomial fit and had a correlation coefficient of at least $R^2 = 0.999$. Based on an uncertainty in the intensity ratio of approximately ± 0.04, the maximum uncertainty in the PSP measurements normalized by p_{inf} was ± 0.08 [16].

Table 1 Microramp dimensions

Quantity	Value
δ	4.77 ± 0.15 mm
A_p	24.0°
h/δ	0.36
c/h	7.20
s/h	7.50
Xp/δ	12.65

A schematic of the experimental setup used for obtaining the PIV images in this investigation is shown in Fig. 2a. Uncertainty in the PIV data velocity measurements is a result of both the capability of the seed to follow the flow and the ability of the imaging and analysis system to record and process the images of the flowfield [17]. A Laskin nozzle was used to seed the main flow with diethylhexyl sebacate (DEHS), which generated particles with a diameter less than 1 μm [18]. The seeding was introduced approximately 3.5 m upstream of the test section, which provided an adequate dispersion of the particles into the freestream flow. The seeding particles had an average lag of 1.8 mm downstream of the normal shock. The average particle lag distance was determined from the instantaneous PIV images of the velocity field near the normal shock. The particles were illuminated by a 0.5-mm-thick light sheet that spanned the distance of each streamwise position, as indicated in Fig. 2b. The uncertainty in the position of the laser sheet in the spanwise direction was approximately ± 0.2 mm. The light sheet was produced by a dual-head New Wave neodymium-doped yttrium aluminum garnet laser in combination with cylindrical and spherical lenses. The laser was operated at 532 nm, with each pulse delivering approximately 40 mJ of energy. The time separation between laser pulses to illuminate the DEHS particles was 676 ns. The pulse timing uncertainty of the laser due to jitter was 1 ns ($w_{t1} = 1$ ns), while the uncertainty of the pulse generator was 1.5 ns ($w_{t2} = 1.5$ ns). The PIV images recorded in the

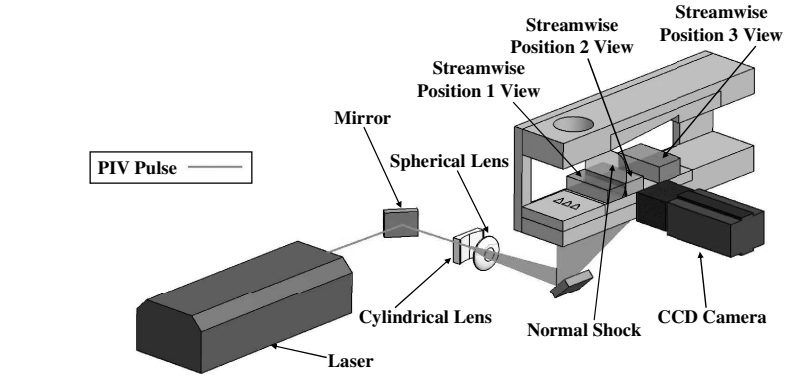

a)

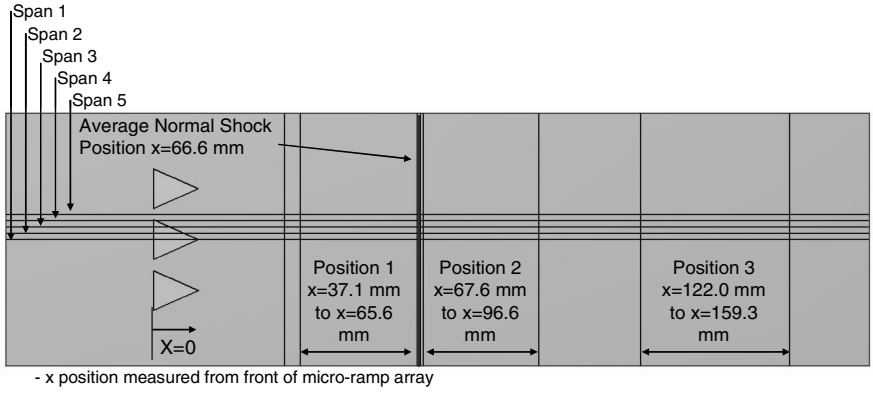

b)

Fig. 2 PIV: a) schematic of setup and b) locations of measurements.

study were obtained with the same CCD camera as described previously, with an image resolution of 1600×640 pixels, and an average scaling magnification of 0.0181 mm/pixel for streamwise positions 1 and 2 and 0.0238 mm/pixel for streamwise position 3. The camera lens was a distance of 0.28 m from the calibration scale location ($d = 0.28$ m), with an uncertainty in position of 1 mm ($w_d = 1$ mm). The length of the scale used for calibration was 7.62 mm ($l = 7.62$ mm), with an accuracy of 10 μm ($w_l = 10$ μm). Uncertainty of pixel locations used in image scaling and image distortions by lens aberrations resulted in uncertainties of 1 pixel ($w_{L1} = 1$ pixel) and 2.1 pixels ($w_{L2} = 2.1$ pixels), respectively. Uncertainties in velocity due to the equipment and calibration procedures used in recording images is given by Eq. (1) and results in a maximum u velocity uncertainty normalized by a freestream velocity of 0.008 [19]:

$$w_{u,\text{equip}} = \sqrt{\left(\frac{\partial u}{\partial l} w_l\right)^2 + \left(\frac{\partial u}{\partial L} w_{L1}\right)^2 + \left(\frac{\partial u}{\partial L} w_{L2}\right)^2 + \left(\frac{\partial u}{\partial d} w_d\right)^2 + \left(\frac{\partial u}{\partial t} w_{t1}\right)^2 + \left(\frac{\partial u}{\partial t} w_{t2}\right)^2} \tag{1}$$

The resulting image pairs were then processed by the dPIV 2.1 software, developed by Innovative Scientific Solutions, Inc., with a one-tenth of a pixel uncertainty in displacement when assuming a Gaussian illumination of the laser sheet. The positional error estimate of approximately 0.1 pixels was achieved by matching the intensity captured from illuminated particles through a Gaussian-shaped peak locator [20]. The average incoming freestream pixel displacement between image pairs was 14.4 pixels, resulting in a maximum u velocity processing uncertainty normalized by a freestream velocity of 0.007. To obtain accurate mean and turbulence properties, large sample sizes of images are required for averaging. Using the approach outlined by Grant and Owens [21], the relative error in the mean velocity due to sampling from 970 images ($N = 970$ images) was estimated at up to 0.007 for a 95% confidence level. These different sources of uncertainty resulted in a maximum total mean u velocity uncertainty of 0.013. The maximum relative error value of the mean velocity was based on the maximum turbulence intensity observed along center spanwise position 1 and streamwise position 1 (discussed next) in the region of the streamwise vortices generated by the center microramp.

Unlike the uncertainty in the mean velocity measurements, turbulent intensities and turbulent stress errors are dominated by statistical convergence errors. The uncertainty of the turbulence intensity was estimated using Eq. (2), while the Reynolds shear stress uncertainty was calculated using Eq. (3). In Eq. (3), the standard deviation in the Reynolds shear stress was calculated using a 95% confidence interval in the scatter of the Reynolds shear stress, both within a single wind-tunnel run and between multiple runs [22]:

$$w_{u'} = u' \frac{z_c}{\sqrt{2N}} \sqrt{1 + 2\left(\frac{u'}{u}\right)^2} \tag{2}$$

$$w_{u'v'} = \frac{\sigma_{u'v'}}{\sqrt{N}} \tag{3}$$

Again, in the region of the streamwise vortices, the maximum uncertainty in the turbulence intensity measurements normalized by

Table 2 Incoming boundary-layer properties

Quantity	Value
δ	4.77 mm
δ^*	0.715 mm
θ	0.545 mm
H	1.31
C_f	0.0020
Π	0.60

the freestream velocity is 0.0048, while the maximum uncertainty in the Reynolds shear stress normalized by the freestream velocity squared is 0.00038 [20–22]. The uncertainty of the Reynolds shear stress is normalized by the freestream velocity in the x direction squared, due to the fact that the mean transverse velocity of the flow is so small. The maximum pixel displacement of the freestream in the y direction is 0.003 pixels and would result in a large Reynolds shear stress uncertainty if it was normalized by both the u and v freestream values.

The PIV images were obtained at three streamwise and five spanwise positions, as displayed in Fig. 2b, for the experimental setup with the microramp array. The diagram in Fig. 2b is a plan view of the xz plane, but the images were obtained in the xy plane at the three streamwise positions for five equally spaced spanwise locations of one symmetry unit of the microramp array from the centerline of the center ramp (span 1) to the plane bisecting the gap to the adjacent ramp (span 5). PIV data for the experimental setup without the microramps were only obtained at spanwise positions 1 and 5 for all three streamwise positions, since the flow is nominally two-dimensional and it was felt unnecessary to obtain measurements at all five spanwise locations. The normal shock is located between streamwise positions 1 and 2, so that streamwise position 1 is downstream of the microramp array while being upstream of the normal shock. Streamwise positions 2 and 3 help to show the effects of the microramp array on the SBLI directly behind the normal shock as well as further downstream, respectively.

III. Results and Discussion

A. Incoming Boundary Layer

PIV measurements of the incoming boundary layer were conducted in order to accurately determine the incoming boundary-layer parameters of the wind-tunnel test section and to determine the correct microramp sizing. The incoming boundary layer is characterized by the values shown in Table 2. The boundary-layer thickness of the incoming flow was determined by the wall-normal distance at 99% of the mean freestream velocity.

A modified wall-wake velocity profile for turbulent compressible boundary layers, as discussed in [23], was fit to the measurements of the incoming boundary layer, as well as to the boundary layer at streamwise position 3, both with and without the microramp array. Because of reflections of the PIV laser sheet along the surface of the wind tunnel, only three streamwise velocity data points are located in the log region of the boundary layer. This can produce uncertainty in the skin friction coefficient calculations, which is why it is only presented to two significant figures rather than three, as specified in [23]. The comparison of the modified wall-wake velocity profile to the experimental measurements for the incoming boundary layer is shown in Fig. 3. The method of least-squares was used to fit the wall-wake profile to the experimental velocity profile. From the fit of the modified wall-wake velocity profile to the experimental data, C_f and the corresponding δ were calculated, as well as the wake strength Π value. The boundary-layer incompressible displacement thickness and momentum thickness were then calculated from their definitions. The resulting velocity profile fit in normalized outer coordinates (y/δ) is shown in Fig. 3a. Figure 3b shows that the incoming boundary-layer profile in wall coordinates is what would be expected for a fully developed compressible turbulent boundary layer, as shown in [24], for comparable Reynolds numbers. The wake strength parameter for the incoming boundary layer is slightly higher, but it is comparable to $\Pi \approx 0.55 \pm 0.05$ for a compressible turbulent boundary layer with $Re_\theta > 2000$ [24]. The skin friction coefficient for the incoming boundary layer is also quite similar to that seen for turbulent compressible boundary layers, as described in [23], and the incompressible shape factor compares well with that for a fully developed turbulent boundary layer at the Reynolds number of the wind-tunnel test section [25].

B. Schlieren Photography

Instantaneous schlieren photographs of the flow without a microramp array in the Mach 1.4 tunnel are shown in Fig. 4. A close up view in Fig. 4b shows that there is no clear evidence of separation due to the normal shock/boundary-layer interaction, but that there is an increase in boundary-layer thickness across the normal shock. The flow is likely incipiently separated. A Mach 1.4 SBLI is usually incipiently separated because the shock strength is not quite high enough to cause full separation. The weak lambda structure of the normal shock also indicates an incipiently separated flow [26]. A weak secondary shock downstream is also present in Fig. 4, showing the transonic nature of the flowfield.

Figure 5 displays instantaneous schlieren photographs of the flow with the microramp array. The boundary layer immediately behind the microramp array apparently thickens in comparison to the incoming boundary layer, and it also produces periodic large-scale structures showing the turbulence created by the vortices generated

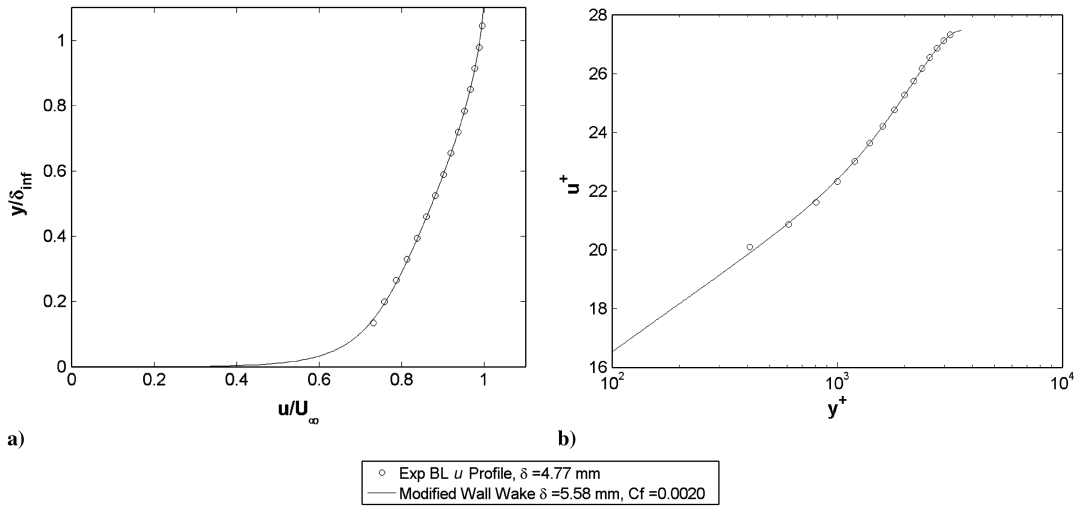

Fig. 3 Measured incoming boundary-layer velocity profile compared with the fit for a modified wall-wake velocity profile: a) in normalized outer coordinates and b) in wall coordinates (BL: boundary layer).

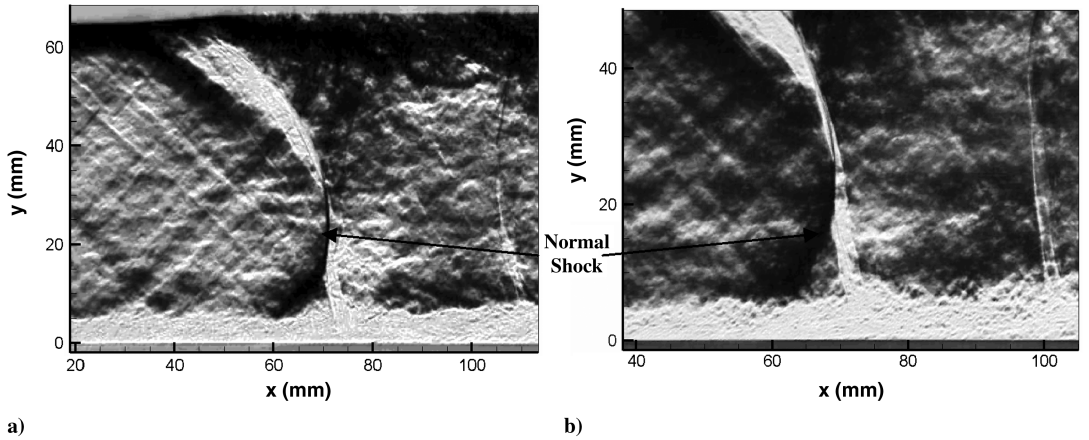

Fig. 4 Instantaneous schlieren photography of normal shock without microramp array: a) wide view and b) zoomed-in view of normal shock/boundary-layer interaction.

by the microramp array. There is an oblique shock produced by the leading edge of the microramp, as well as one produced at the trailing edge. The latter shock is most likely due to the increase in boundary-layer thickness after the microramp array. The increase in the boundary-layer thickness will affect the necessary geometry of a supersonic inlet when compared with traditional inlet designs using a bleed system for boundary-layer control.

Comparing Figs. 4 and 5, it appears that the boundary layer is thicker after the normal shock with the microramp array in the flow than without it in the flowfield. There also does not appear to be any clear evidence of separation of the flow, and it is likely incipiently separated with the microramp array as well as without the microramp array. The only difference is that the lambda structure of the normal shock with the microramp array appears narrower in the streamwise direction than that without the microramp array, indicating an even weaker propensity for separation with the microramp array.

C. Surface Flow Visualization

A surface flow visualization photograph of the microramp array is shown in Fig. 6. The streaklines past the trailing edges of each microramp show how the microramp creates two large counter-rotating vortices: one on each side. The darker areas are indicative of the high-momentum flow of these vortices along the surface of the wind tunnel. The surface flow visualization also shows how the flow curves over the edges of the front face of the microramp, creating the vortices as this flow separates from the ramp. The two large vortices along the trailing edges of the microramp are shown by the small amount of oil left just behind the two trailing edges. This oil also shows that there might be smaller secondary counter-rotating vortices created along with the larger main vortices. At the very tip of the trailing edge, there is a deposit of oil, indicating that the flow has separated there; but a little downstream of this, the large vortices come together, showing another region of high momentum along the

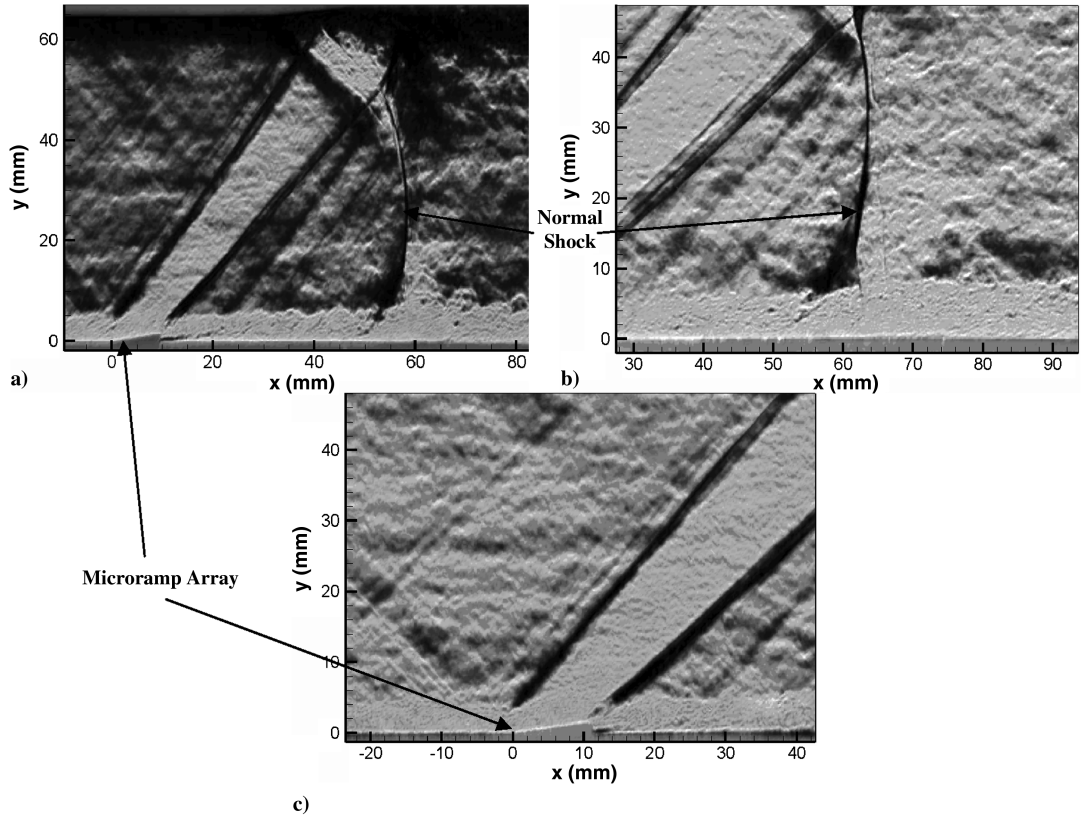

Fig. 5 Instantaneous schlieren photography of normal shock with microramp array: a) wide view, b) zoomed-in view of normal shock/boundary-layer interaction, and c) zoomed-in view of microramp array.

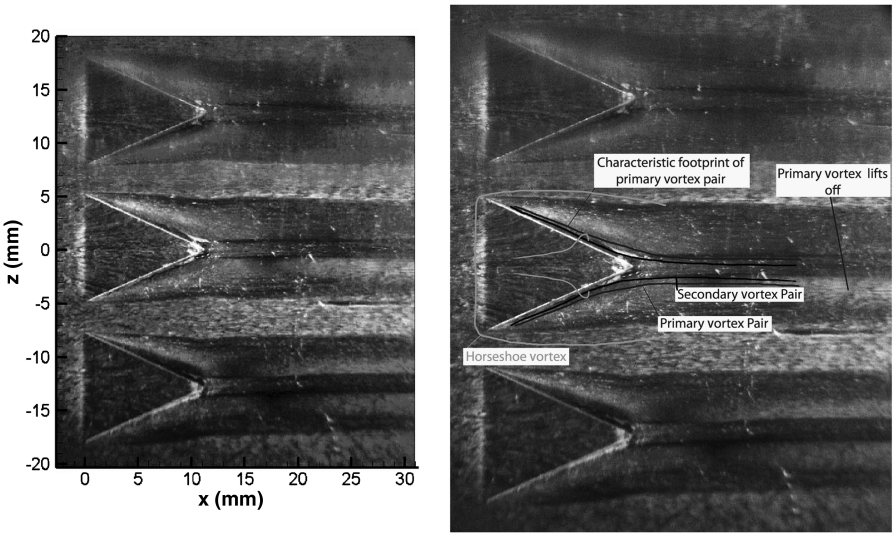

Fig. 6 Microramp array: a) surface flow visualization and (b) surface flow visualization with features marked.

wall surface. The flow to either side of each microramp appears to be relatively unaffected, indicating that an array of microramps is necessary to have a substantial effect on the flow in a supersonic inlet. Each microramp in the array has similar surface flow characteristics, showing that the flow at the microramps is unaffected by neighboring microramps, and the flow appears to be symmetric over each microramp. The prominent features of the surface flow are marked in Fig. 6b (as also shown in [13]). The high-momentum regions show that the flow near the surface is energized by the microramp, indicating that it may indeed help with separation after a shock/boundary-layer interaction. A potential problem is that the schlieren images seem to indicate an increase in the boundary-layer thickness downstream of the microramp array, demonstrating that these high-momentum vortices start to lift off the surface the further downstream they propagate from the array.

The surface flow visualization of the normal shock/boundary-layer interaction region is displayed in Fig. 7, both with and without the microramp array. Figure 7 confirms what was seen by schlieren photography, in that the flow is apparently incipiently separated due to the normal shock/boundary-layer interaction, both with and without the microramp array. In Fig. 7b, the effects of the microramp array (particularly, the counter-rotating vortices) can be seen leading into the normal shock, but the vortices do not appear to have much of an effect on the surface flow, indicating that the vortices have likely started to lift off the surface the further they travel from the microramp array, as also seen with the schlieren photography.

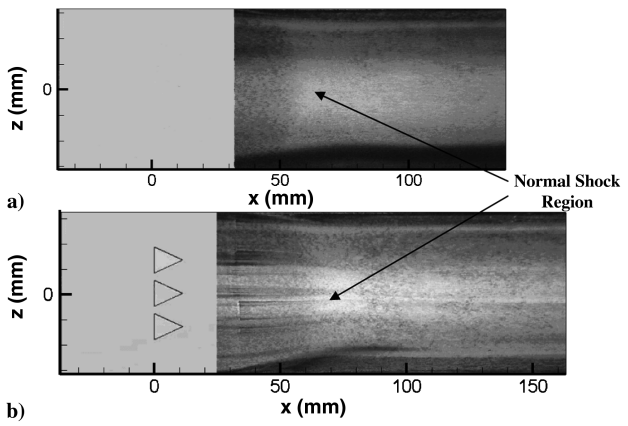

Fig. 7 Surface flow visualization of normal shock wave: a) without microramp array and b) with microramp array.

D. Pressure-Sensitive Paint

Figure 8 depicts the PSP measurements of the microramp array with the locations of the calibration pressure taps indicated as black dots.

The pressure distributions around each microramp are very similar. There is a pressure increase on the forward face where the oblique shock generated by the ramp originates. The pressure starts to decrease as the flow moves up the forward face, and the primary vortices are generated, leaving a pressure deficit on the trailing edges. There is also a peak in pressure directly behind the trailing point of each microramp generated by the vortices.

Figure 9a shows the pressure profiles along five equally spaced spans in one symmetry unit from the middle of the center microramp (span 1) to the middle of the gap between ramps (span 5). Span 1 shows the pressure increase on the upstream portion of the forward face as well as the decrease in pressure on the forward face as the flow moves further downstream generating the counter-rotating vortices on both sides of the microramp. Span 2 shows the greatest pressure drop along the trailing edge of the side of the microramp. Since the trailing edge moves further upstream as the spans increase in number, the pressure drop also moves further upstream until spans 4 and 5. At spans 4 and 5, there is less of a pressure increase and drop due to the

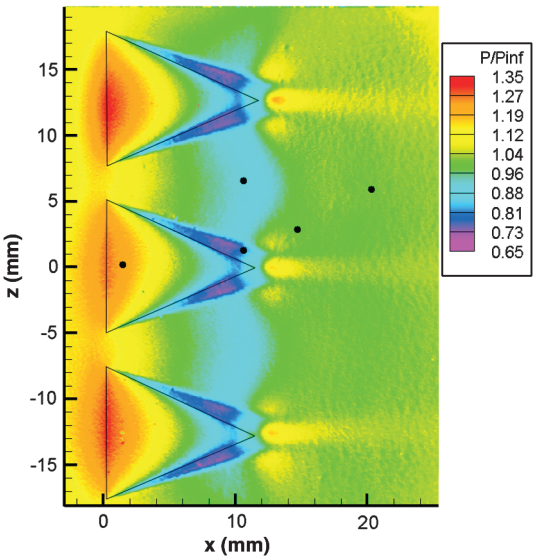

Fig. 8 PSP measurements of microramp array with pressure-tap locations.

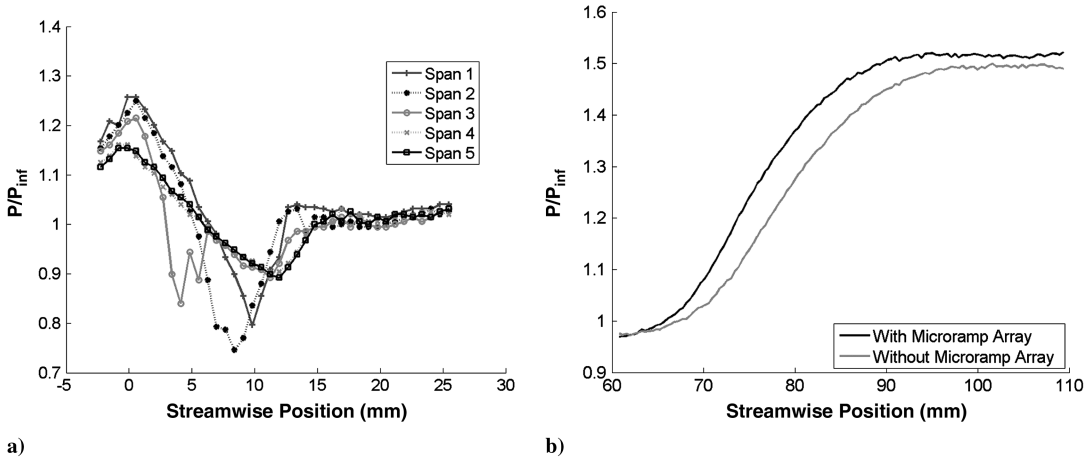

Fig. 9 Streamwise pressure distributions for a) five equally spaced spans within one symmetry unit across the microramp array and b) across normal shock, both with and without microramp array.

fact that span 4 is along the edge of the microramp and span 5 is in between the microramps.

Figure 9b displays line plots of the streamwise pressure distributions with and without the array from the PSP measurements located at the normal shock/boundary-layer interaction. Again, the coordinate system is displayed, showing the flow going left to right. Pressure-tap measurements were made with five taps spaced down the centerline of the tunnel. As would be expected for the pressure distribution across a normal shock wave, Fig. 9b shows a large increase in pressure across the shock. In Fig. 9b, the effects of the microramp array can clearly be seen. Figure 9b reveals better static pressure recovery with the microramp array than without, and the shock is also shifted slightly upstream with the array. The streamwise pressure distributions shown are the spanwise-averaged values across all the spans in one symmetry unit of the microramp array.

E. Particle Image Velocimetry

Figure 10 presents the mean velocity in the x direction for all three streamwise positions, with Figs. 10a–10c displaying spanwise position 1 (centerline) without the microramp array and Figs. 10d–10i with the microramp array for spanwise positions 1 (centerline of

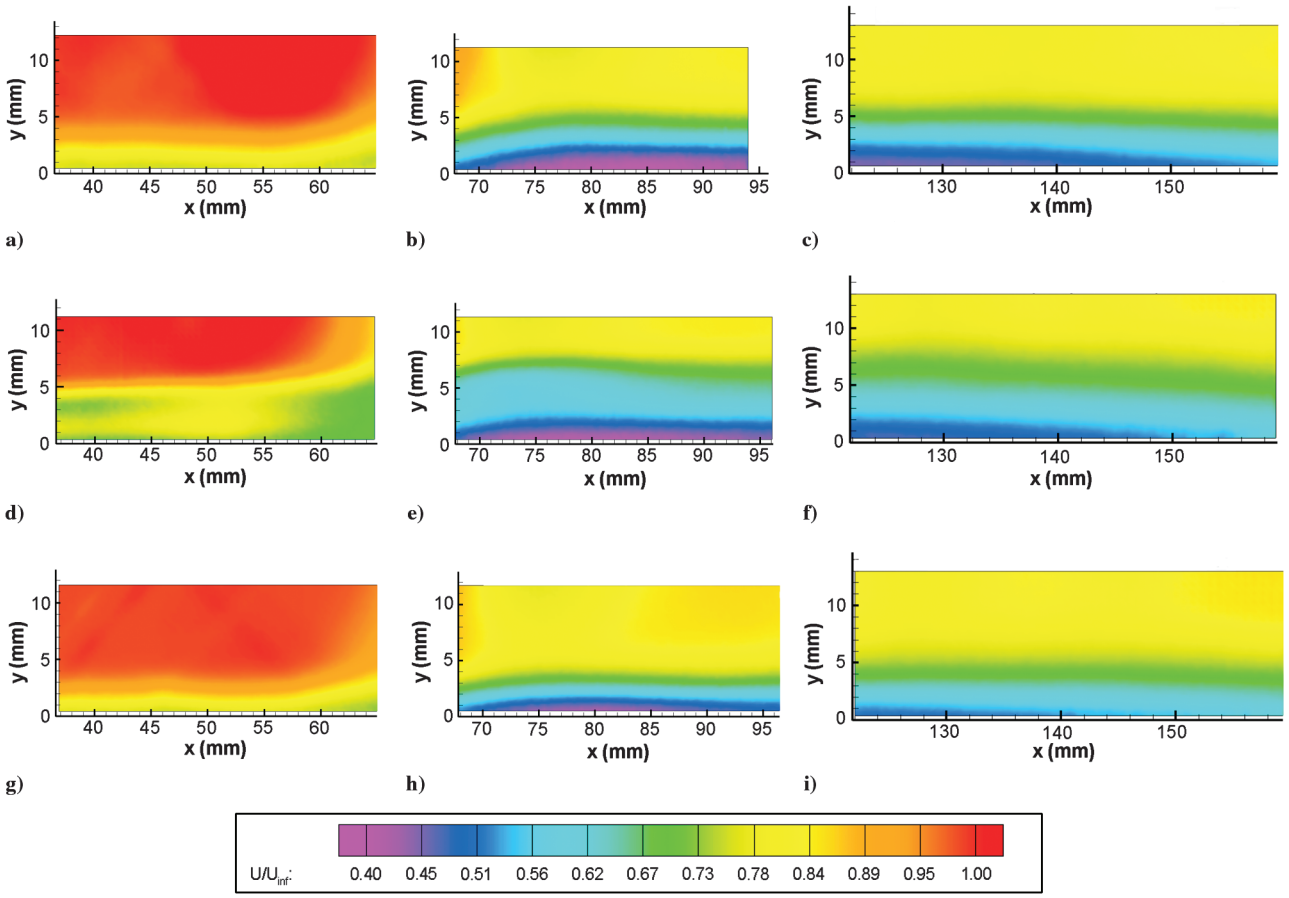

Fig. 10 Average u velocity without microramp array: a) streamwise position 1/spanwise position 1, b) streamwise position 2/spanwise position 1, and c) streamwise position 3/spanwise position 1. Average u velocity with microramp array: d) streamwise position 1/spanwise position 1, e) streamwise position 2/spanwise position 1, f) streamwise position 3/spanwise position 1, g) streamwise position 1/spanwise position 5, h) streamwise position 2/spanwise position 5, and i) streamwise position 3/spanwise position 5.

center ramp) and 5 (centerline of the adjacent ramp gap), respectively. The normal shock lies between streamwise positions 1 and 2, while the distance between streamwise positions 2 and 3 is larger than the distance between streamwise positions 1 and 2. The effects of the shock can be seen at the downstream end of streamwise position 1 and at the upstream end of streamwise position 2. The spanwise position 5 data without the microramp array are not presented here, since the flow is nominally two-dimensional.

Figures 10a, 10d, and 10g show how the microramp array increases the boundary-layer thickness directly behind the center span of the microramp array (spanwise position 1) compared with the flow without the microramp array. However, it appears that the boundary-layer thickness has decreased for the span in between microramps of the array (spanwise position 5) with the microramp array as compared to the case without it. The PIV data in Fig. 10 show no clear evidence of flow separation, and the boundary layer is likely incipiently separated due to the normal shock/boundary-layer interaction, both with and without the microramp array, as shown by the schlieren and surface flow visualization measurements. The flowfields displayed in Figs. 10b, 10e, and 10h (streamwise position 2) show how the boundary-layer thickness increases due to the normal shock, but there is still a thicker boundary layer directly downstream of the ramp, but thinner between ramps, as compared with the no-array case. The boundary layer is clearly redeveloping as it moves downstream to streamwise position 3, as displayed by Figs. 10c, 10f, and 10i, since these figures reveal that higher-momentum flow is moving closer to the wall as it moves further downstream from the normal shock.

Figure 11 shows yz end views of the average u velocity with the microramp array for streamwise position 1 at $x = 50$ mm, position 2 at $x = 88$ mm, and position 3 at $x = 153$ mm to help display the three-dimensional effects of the microramps. Since measurements were obtained at only five spanwise positions, or five z positions, the resulting contour plots rely heavily on interpolation and sometimes have sharp peaks, as can be seen. Figure 12 shows the raw data locations of the yz end view before interpolation for streamwise position 1. The data locations for streamwise positions 2 and 3 are similar to those for position 1. For clarity in the plot, the data for the five spanwise positions were reflected across the $z = 0$ axis in the plot, since this is a nominally symmetric flow. The outline of the center microramp is also sketched in each figure.

Figure 11 helps to further show the results seen in Fig. 10. At streamwise position 1 (Fig. 11a), there is a region of low-momentum flow directly above the ramp but higher-momentum flow near the edges of the microramp. The height of this low-momentum flow reveals how the generated vortices lift off the surface the further downstream they move from the microramp. The effects of the

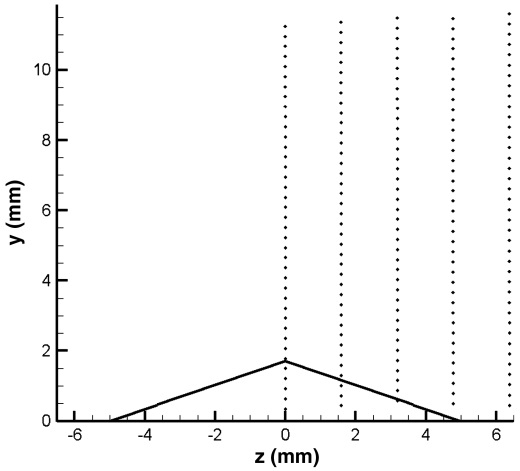

Fig. 12 Raw data locations for the yz end view of flowfield before interpolation at streamwise position 1.

vortices are seen in Figs. 11b and 11c as well, but the effects are less prominent due to the redeveloping boundary layer approaching equilibrium after its interaction with the normal shock. At the edges of Fig. 11c, there is an area of lower-momentum flow further from the surface, as seen in the middle of the flow where the effects of the vortices are greatest. This area of lower-momentum fluid is likely due to the diffusion and expansion of the vortices as they move downstream.

Figure 13 shows the u' turbulence characteristics of the flowfield in the same arrangement shown in Fig. 10. There appears to be a high u' turbulence region created by the primary vortices of the microramp array, as seen in Fig. 13d. The vortices are generated at the center span of the array, directly behind the microramp, and are not present at the span in between microramps. The normal shock also increases u' at each span, with and without the microramp array, as expected. The u' turbulence is greatest for a further distance from the surface of the tunnel at spanwise position 1 with the microramp array, again indicating that it has a larger boundary-layer thickness. At streamwise position 3, the u' turbulence is more uniform along all spans, both with and without the microramp array. At this most downstream position, the boundary layer appears to be thinner and less turbulent on the plane between ramps (Fig. 13i) than for the case with no array (Fig. 13c). The v' data are not presented here, because the trends are similar to those for the u' data.

The yz end views of u' in Fig. 14 show how the vortices generated by the microramp start to merge and lift off the surface the further

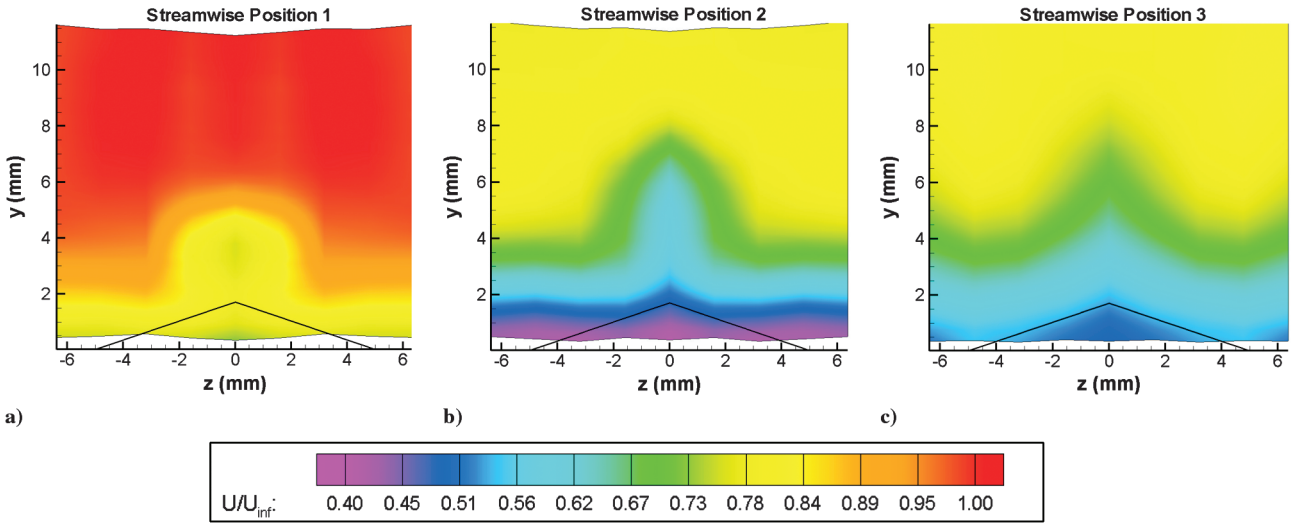

Fig. 11 Average u velocity yz end views of flowfield for all three streamwise positions with the microramp array: a) $x = 50$ mm, b) $x = 88$ mm, and c) $x = 153$ mm.

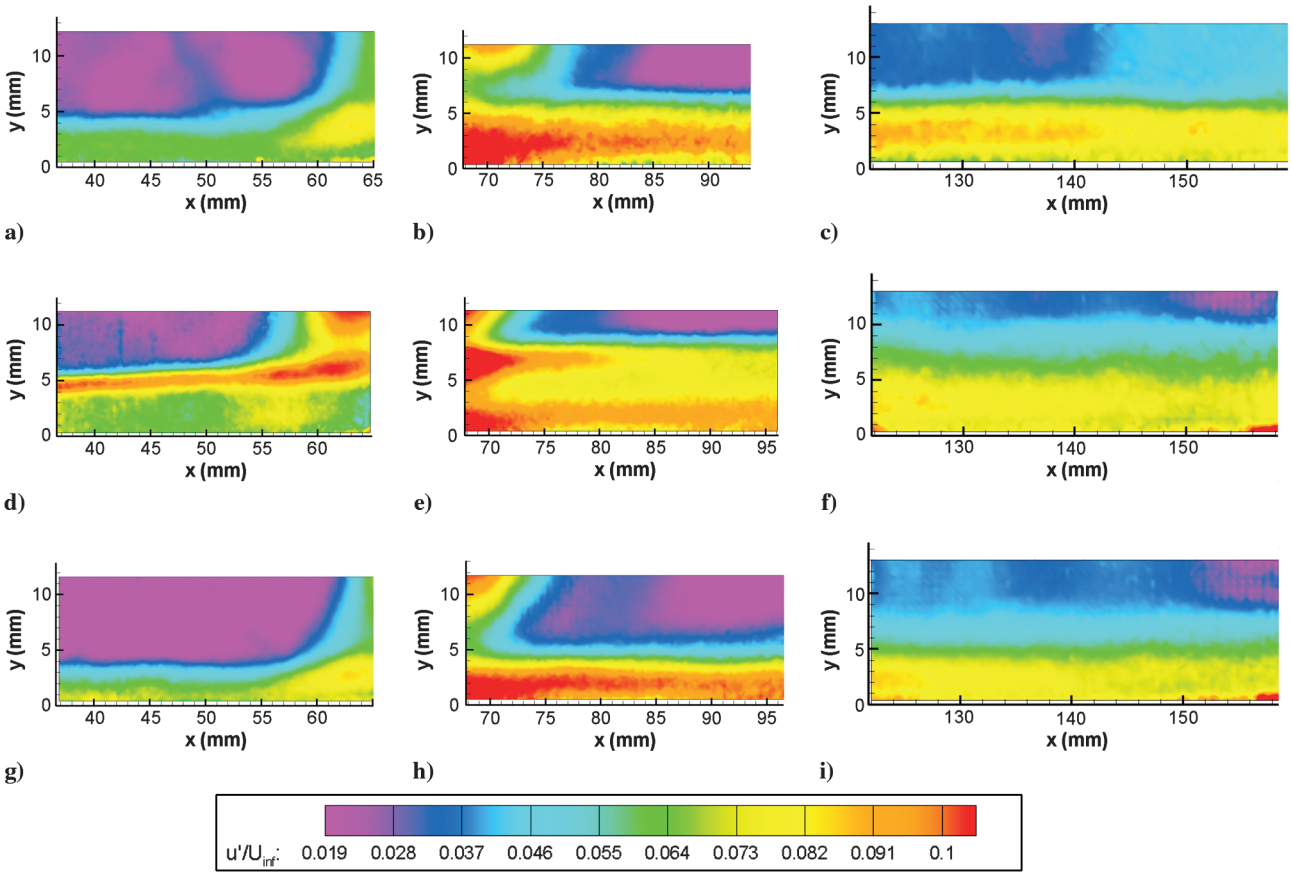

Fig. 13 The u' velocity without microramp array: a) streamwise position 1/spanwise position 1, b) streamwise position 2/spanwise position 1, and c) streamwise position 3/spanwise position 1. The u' velocity with microramp array: d) streamwise position 1/spanwise position 1, e) streamwise position 2/spanwise position 1, f) streamwise position 3/spanwise position 1, g) streamwise position 1/spanwise position 5, h) streamwise position 2/spanwise position 5, and i) streamwise position 3/spanwise position 5.

they move downstream. The turbulence generated by the microramps is still localized after the normal shock, as displayed in Fig. 14b, but has increased in uniformity across the z span further downstream of the normal shock, with a decrease in magnitude, as demonstrated in Fig. 14c. This indicates that the boundary layer is redeveloping, and that the effects of the microramp array have spread across all of the spanwise positions downstream of the normal shock.

The Reynolds shear stress ($u'v'$) of the flowfield is displayed in Figs. 15 and 16. The large-scale turbulent structures of the vortices generated along the microramp centerline are shown quite clearly in Fig. 15d (by the large $u'v'$ values), and Fig. 15e shows that these structures/vortices do continue through the normal shock, but they are reduced in strength (i.e., peak shear stress) and appear quite weak at streamwise position 3, as shown by Figs. 15f and 16c. The Reynolds shear stress of spanwise position 1 without the microramp array at a given streamwise position is very similar to that at spanwise position 5 with the microramp array. The largest difference is seen at streamwise position 3, where there is a larger Reynolds shear stress in

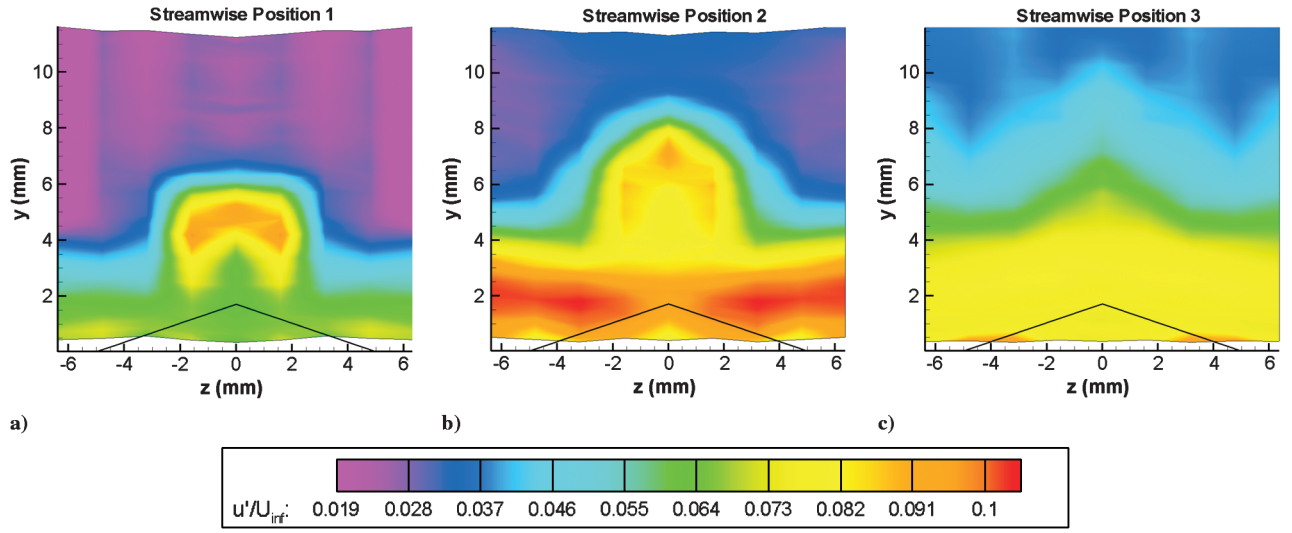

Fig. 14 The u' velocity yz end views of flowfield for all three streamwise positions with the microramp array: a) $x = 50$ mm, b) $x = 88$ mm, and c) $x = 153$ mm.

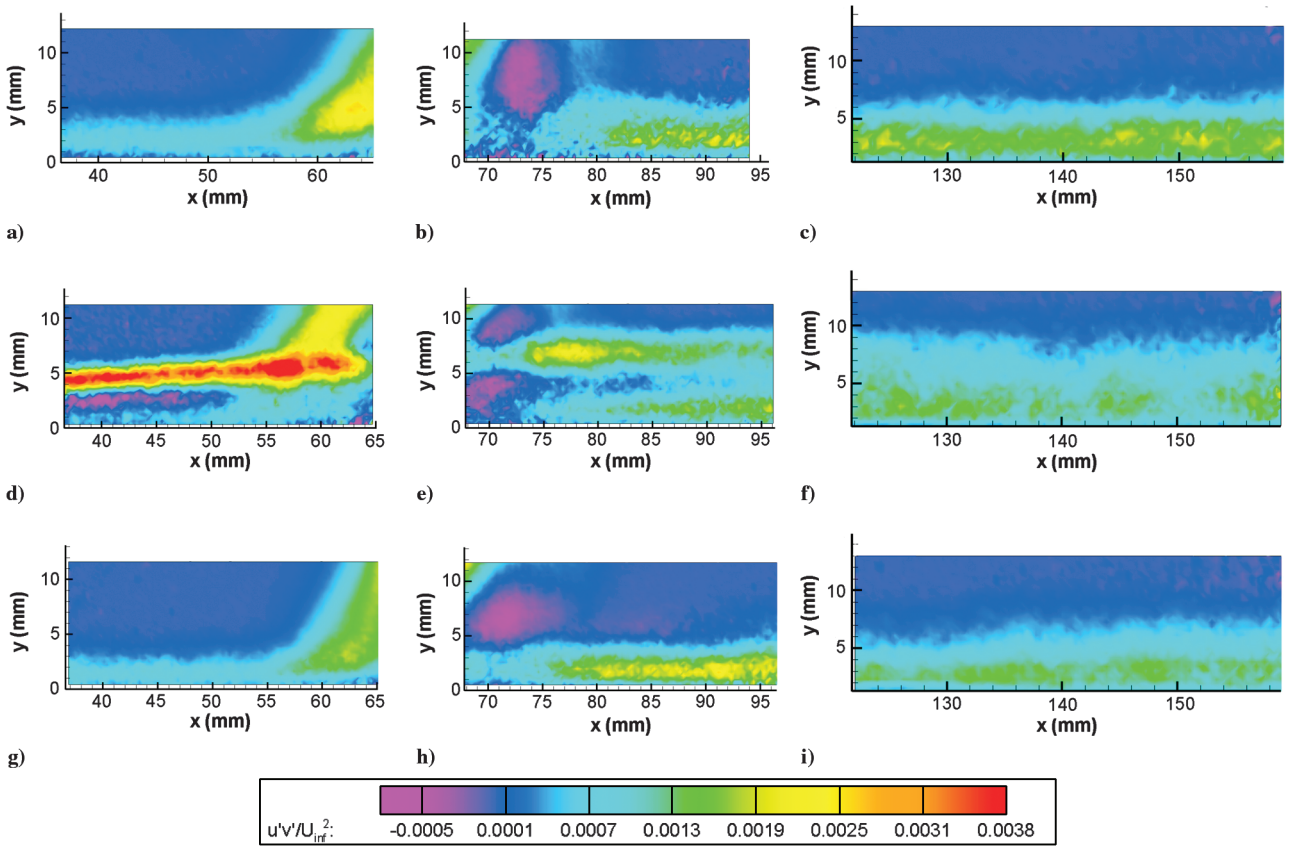

Fig. 15 Reynolds shear stress without microramp array: a) streamwise position 1/spanwise position 1, b) streamwise position 2/spanwise position 1, and c) streamwise position 3/spanwise position 1. Reynolds shear stress with microramp array: d) streamwise position 1/spanwise position 1, e) streamwise position 2/spanwise position 1, f) streamwise position 3/spanwise position 1, g) streamwise position 1/spanwise position 5, h) streamwise position 2/spanwise position 5, and i) streamwise position 3/spanwise position 5.

the boundary layer closer to the surface for the case without the microramp array (Fig. 15c).

To clarify the proceeding velocity contours, Fig. 17 displays the boundary-layer profiles of the average u velocity, u', v', and Reynolds shear stress at spanwise positions 1 and 5, both with and without the microramp array. These boundary-layer profiles are the profiles measured at $x = 50$ mm for position 1, $x = 88$ mm for position 2, and $x = 153$ mm for position 3. Figure 17 shows quantitatively how the boundary layer is thicker with the microramp on the microramp centerline (span 1), as seen with earlier results. It also displays that the boundary-layer thicknesses for the cases with and without microramps along span 5 are nearer to each other than for span 1 on the microramp centerline.

Figures 17a shows that there is a small effect of increased mean velocity/momentum near the wall due to the microramp array. The vortices generated along the microramp array centerline can be seen in each of the flow characteristics in Fig. 17, but it is also shown how their effect decreases as the flow moves through the normal shock and

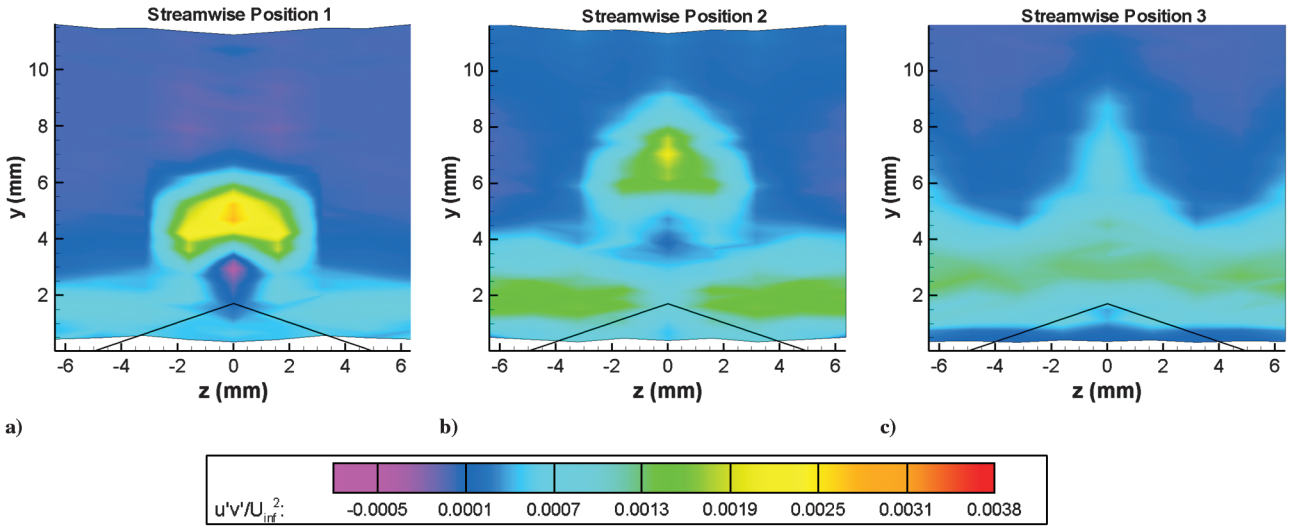

Fig. 16 Reynolds shear stress *yz* end views of flowfield for all three streamwise positions with the microramp array: a) $x = 50$ mm, b) $x = 88$ mm, and c) $x = 153$ mm.

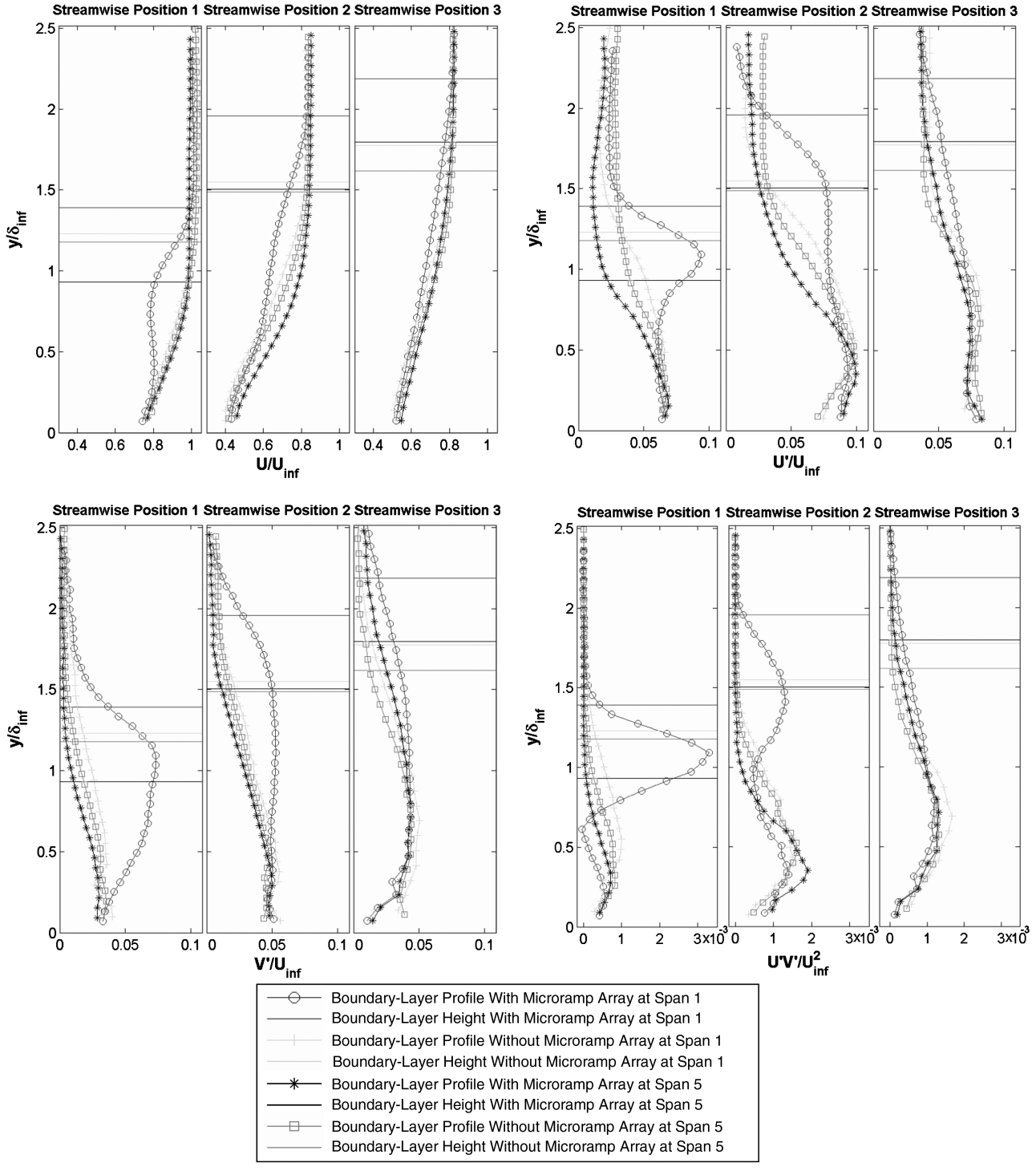

Fig. 17 Boundary-layer profiles at spanwise positions 1 and 5 for streamwise position 1, $x = 50$ mm; streamwise position 2, $x = 88$ mm; and streamwise position 3, $x = 153$ mm, both with and without microramp array for a) average u velocity, b) u', c) v', and d) Reynolds shear stress ($u'v'$).

further downstream. It does not appear that the microramps have a significant effect further downstream of the normal shock and that their effect is mainly present near the microramp array.

Again, in Fig. 17 it can be seen, as in the contour plots, that the boundary-layer thickness at streamwise position 1/spanwise position 1 is thicker with microramps than without, but at streamwise position 1/spanwise position 5, the boundary layer is thicker without microramps than with. Figure 17d shows how the primary vortices of the microramp do lift off the surface the further the flow moves downstream. This is quite clear when comparing streamwise positions 1 and 2. The effect of the vortices can be seen at streamwise position 3 (see Figs. 11c, 14c, and 16c), at a location further from the wall than at position 2, but their effects are substantially less prominent. Figure 17d also shows how the maximum Reynolds shear stress without the microramp array is usually closer to the wall than that for the case with the array at spanwise position 1, while the Reynolds shear stress profile is very similar between the cases with and without the array at spanwise position 5. The main differences in the Reynolds shear stress profiles, between the case with and without the array at spanwise position 5, is that the maximum Reynolds shear stress is slightly further from the wall without the array than with the array at streamwise positions 1 and 2, unlike at streamwise position 3. Table 3 lists the boundary-layer thicknesses for each of the boundary-layer profiles shown in Fig. 17.

Table 3 Boundary-layer thicknesses

Streamwise position	Spanwise position 1, mm	Spanwise position 5, mm
1 with array	6.64	4.44
2 with array	9.34	7.18
3 with array	10.44	8.57
1 without array	5.86	5.63
2 without array	7.38	7.10
3 without array	8.47	7.72

Table 4 Boundary-layer properties at streamwise position 3 ($x = 153$ mm)

Quantity	Average spanwise value with array	Spanwise value without array
δ	8.80 mm	8.47 mm
δ^*	1.44 mm	1.67 mm
θ	1.07 mm	1.16 mm
H	1.34	1.44
C_f	0.0017	0.0014

The modified wall-wake velocity profile described earlier for the incoming boundary layer was also applied to the boundary-layer profiles for streamwise position 3 at each spanwise position, both with and without the microramp array. The use of the modified wall-wake velocity profile at streamwise position 3 was felt justified due to the similarity of the boundary-layer velocity profiles in wall coordinates at streamwise position 3 and the incoming boundary layer. Since the flow is nominally two-dimensional without the microramp array, the values for only spanwise position 1 are presented. When comparing the fitted boundary-layer thicknesses to the experimental results, the largest percent difference is 17%, which means that there is a reasonable correlation between the fitted wall-wake velocity profile and the experimental data. We also note that the boundary-layer thickness determined directly from the experimental data is the 99% velocity thickness, while that determined from the Sun and Childs [23] curve fit corresponds to approximately the 99.5% velocity thickness.

Figure 18 presents the integral boundary-layer properties at streamwise position 3 for all five spanwise positions with the array and at spanwise position 1 without the array. Table 4 lists the spanwise-averaged values of these same properties at streamwise position 3, both with and without the microramp array. From Fig. 18a, it can be seen that the boundary-layer thickness is greater at spanwise positions 1 and 2 with the microramp array than without, while the displacement thickness and momentum thickness were greater with the microramps than without them only at spanwise position 1 on the microramp centerline. Table 4 shows that the spanwise-averaged value of the boundary-layer thickness is greater with the array, while the average displacement and momentum thicknesses are less than without the array.

Figure 18b and Table 4 show that the boundary layer at streamwise position 3 is closer to separation without the microramp array, based both on the incompressible shape factor and skin friction coefficient at all five spanwise positions. This is shown by the fact that the incompressible shape factor with the array is always less than without the array, while the skin friction coefficient with the array is always larger than without the microramp array. These results show that the microramp array does indeed improve the boundary-layer health downstream of the normal shock/boundary-layer interaction and can help resist boundary-layer separation in stronger SBLIs.

IV. Conclusions

A microramp array has been examined at Mach 1.4, and its effects on normal SBLIs have been investigated. The flow over the array has been described in detail. At the trailing edge of the microramps, separation occurs, forming a counter-rotating primary vortex pair. The primary vortex pair lifts off the surface as it moves downstream, entraining higher-momentum fluid into the boundary layer. The effects of the microramps are most obvious in the region directly downstream of the microramps. The primary vortices do persist through the normal shock, but they are substantially reduced in strength. The vortices are all but dissipated by the most downstream observation location examined here, and they appear to be spanwise localized to the region directly behind the microramps and are not apparent in the regions between the microramps in the array. This necessitates the use of an array of microramps for large-scale inlet flow control. The normal shock was apparently not strong enough to induce large-scale boundary-layer separation in the current experiments. It was therefore not possible to determine the effectiveness of the microramp array in resisting separation in these experiments. The microramp array did increase the spanwise-averaged boundary-layer thickness downstream of the SBLI. However, the microramp array increases flow momentum near the surface, as shown by a decrease in the spanwise-averaged values of δ^*, θ, and H, and an increase in C_f relative to the case with no array. This indicates that microramps can definitely improve the health of the boundary layer and could resist separation in stronger SBLIs. Microramps may thus be employed to augment or possibly replace bleed in the design of future supersonic inlets, thereby reducing drag and improving aircraft performance.

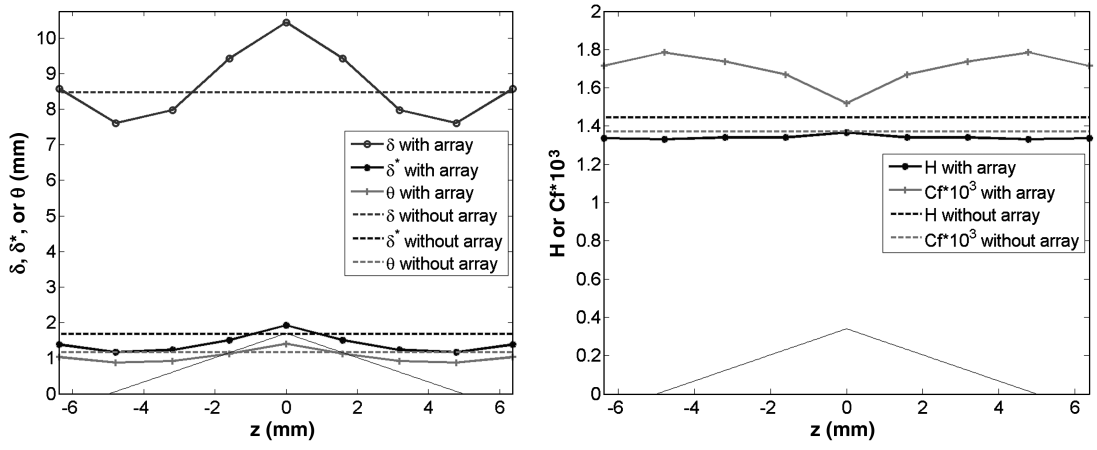

a) b)

Fig. 18 Boundary-layer properties at streamwise position 3 ($x = 153$ mm) for all spanwise positions with and without the microramp array: a) boundary-layer thickness, incompressible displacement thickness, and incompressible momentum thickness; and b) incompressible shape factor and skin friction coefficient.

Acknowledgments

The authors would like to thank Rolls–Royce, plc., and Gulfstream for funding this work on small-scale two-dimensional microramp effects. Any opinions, findings, and conclusions or recommendations expressed in this material are those of the authors and do not necessarily reflect the views of Rolls–Royce, plc., and Gulfstream. Additionally, we would like to thank our colleagues, Eric Loth at the University of Illinois, Tim Conners, Robbie Cowart, and Tom Wayman at Gulfstream, and Rod Chima, Jim Debonis, and Stefanie Hirt at NASA for their discussions and input regarding this work.

References

[1] Bodner, J. P., Davis, D. O., Gerber, I., and Hingst, W. R., "Experimental Investigation of the Effect of a Single Bleed Hole on a Supersonic Turbulent Boundary-Layer," AIAA Paper 1996-2797, July 1996.

[2] Aktinson, M. D., "Numerical Investigation of a Super-Sonic Inlet Using Bleed and Micro-Ramps to Control Shock-Wave/Boundary Layer Interactions," AIAA Paper 2007-0024, 2007.

[3] Chokani, N., and Squire, L. C., "Transonic Shockwave/Turbulent Boundary Layer Interactions on a Porous Surface," *The Aeronautical Journal*, Vol. 97, No. 965, May 1993, pp. 163–170.

[4] Stanewsky, E., "Aerodynamic Benefits of Adaptive Wing Technology," *Aerospace Science and Technology*, Vol. 4, No. 7, 2000, pp. 439–452. doi:10.1016/S1270-9638(00)01069-5

[5] Smith, A., Babinsky, H., Fulker, J., and Ashill, P., "Experimental Investigation of Transonic Aerofoil Shock/Boundary Layer Interaction Control Using Streamwise Slots," *Proceedings of Fluid Mechanics and Its Applications, IUTAM Symposium Transsonicum IV*, edited by H. Sobieczky, Kluwer, Dordrecht, The Netherlands, 2002, pp. 285–290.

[6] Smith, A., Babinsky, H., Fulker, J., and Ashill, P., "Control of Normal Shock Wave/Turbulent Boundary-Layer Interaction Using Streamwise Slots," AIAA Paper 2001-0739, Jan. 2001.

[7] Holden, H. A., and Babinsky, H., "Separated Shock–Boundary-Layer Interaction Control Using Streamwise Slots," *AIAA Journal*, Vol. 42, No. 1, Jan.–Feb. 2005, pp. 166–171. doi:10.2514/1.4687

[8] Babinsky, H., and Ogawa, H., "Three-Dimensional SBLI Control for Transonic Airfoils," 3rd AIAA Flow Control Conference, AIAA Paper 2006-3698, 5–8 June 2006.

[9] Ashill, P. R., Fulker, J. L., and Hackett, K. C., "Research at DERA on Sub Boundary Layer Vortex Generators (SBVGs)," AIAA Paper 2001-0887, 2001.

[10] Anderson, B., Tinapple, J., and Surber, L., "Optimal Control of Shock Wave Turbulent Boundary Layer Interactions Using Micro-Array Actuation," AIAA Fluids Engineering Conference, AIAA Paper 2006-3197, June 2006.

[11] Lee, S., Loth, E., and Wang, C., "LES of Supersonic Turbulent Boundary Layers with μVG's," AIAA Paper 2007-3916, 2007.

[12] Holden, H., and Babinsky, H., "Effect of Microvortex Generators on Separated Normal Shock/Boundary Layer Interactions," *Journal of Aircraft*, Vol. 44, No. 1, Jan.–Feb. 2007, pp. 170–174. doi:10.2514/1.22770

[13] Pitt Ford, C. W., and Babinsky, H., "Micro-Ramp Control for Oblique Shock Wave/Boundary Layer Interactions," AIAA Paper 2007-4115, 2007.

[14] Shinn, A. F., Vanka, S. P., Mani, M., Dorgan, A., and Michal, T., "Application of BCFD Unstructured Grid Solver to Simulation of Micro-Ramp Control of Shock/Boundary Layer Interactions," 25th AIAA Applied Aerodynamics Conference, AIAA Paper 2007-3914, 25–28 June 2007.

[15] Babinsky, H., Li, Y., and Pitt Ford, C. W., "Microramp Control of Supersonic Oblique Shock-Wave/Boundary-Layer Interactions," *AIAA Journal*, Vol. 47, No. 3, March 2009, pp. 668–675. doi:10.2514/1.38022

[16] Woodmansee, M. A., and Dutton, J. C., "Treating Temperature-Sensitivity Effects of Pressure-Sensitive Paint and Associated Wind Tunnel Data Reduction Methods," M.S. Thesis, Univ. of Illinois at Urbana-Champaign, Urbana, IL, 1997.

[17] Urban, W. D., and Mungal, M. G., "Planar Velocity Measurements in Compressible Mixing Layers," *Journal of Fluid Mechanics*, Vol. 431, 2001, pp. 189–222. doi:10.1017/S0022112000003177

[18] Humphreys, W. M., and Bartram, S. M., "Measurement of Separating Flow Structures using a Multiple-Camera DPIV System," *19th International Congress on Instrumentation in Aerospace Simulation Facilities*, IEEE Publ., Piscataway, NJ, 2001, pp. 82–93.

[19] Lazar, E., DeBlauw, B., Glumac, N., Dutton, C., and Elliott, G., "A Practical Approach to PIV Uncertainty Analysis," AIAA Paper 2010-4355, 2010.

[20] Huffman, R., "An Experimental Investigation into the Effect of Plasma on the Flow Features of an Axisymmetric Jet," Ph.D. Dissertation, Univ. of Illinois, Urbana-Champaign, IL, 2007.

[21] Grant, I., and Owens, E., "Confidence Interval Estimates in PIV Measurements of Turbulence Flows," *Applied Optics*, Vol. 29, No. 10, 1990, pp. 1400–1402. doi:10.1364/AO.29.001400

[22] Beresh, S. J., Henfling, J. F., Erven, R. J., and Spillers, R. W., "Turbulent Characteristics of a Transverse Supersonic Jet in a Subsonic Compressible Crossflow," *AIAA Journal*, Vol. 43, No. 11, 2005, pp. 2385–2394. doi:10.2514/1.14575

[23] Sun, C. C., and Childs, M. E., "A Modified Wall Wake Velocity Profile for Turbulent Compressible Boundary Layers," *Journal of Aircraft*, Vol. 10, No. 6, June 1973, pp. 381–383. doi:10.2514/3.44376

[24] Fernholz, H. H., and Finley, P. J., "A Critical Commentary on Mean Flow Data for Two-Dimensional Compressible Turbulent Boundary Layers," AGARD AGARDograph Rept. 223, 1980.

[25] Fernholz, H. H., and Finley, P. J., "Incompressible Zero-Pressure-Gradient Turbulent Boundary Layers: An Assessment of the Data," *Progress in Aerospace Sciences*, Vol. 32, No. 4, 1996, pp. 245–311. doi:10.1016/0376-0421(95)00007-0

[26] Carroll, B. F., "A Numerical and Experimental Investigation of Multiple Shock Wave/Turbulent Boundary Layer Interactions in a Rectangular Duct," Ph.D. Dissertation, Mechanical and Industrial Engineering Department, Univ. of Illinois at Urbana-Champaign, Urbana, IL, 1988.

E. Gutmark
Associate Editor